Experimental and Modeling Study of RF Performance of a Screen-Printed Coplanar Waveguide (CPW) up to 20 GHz Under Monotonic Stretching

Yi Zhou, Justin H. Chow, Manos M. Tentzeris, *Fellow, IEEE*, and Suresh K. Sitaraman

***Abstract*— To meet the increasing need of wireless communication, radio frequency (RF) modules are commonly included in the design of flexible hybrid electronics (FHE). The reliability of printed flexible electronics under deformation has been widely studied under direct current (dc) conditions, while limited studies have been conducted under RF conditions. This work provides insight into how monotonic stretching changes the RF performance at a frequency range of 2–20 GHz of a coplanar waveguide (CPW) transmission line. The CPW is a silver ink screen-printed on a polyethylene terephthalate (PET) substrate, with a thin encapsulation on top of the silver conductor. The sample is subjected to monotonic stretching at a rate of 10 mm/min up to 70% strain, while in situ scattering parameters (S-parameters) are recorded by a vector network analyzer (VNA). Greater changes are observed in the insertion loss than in the return loss as the CPW undergoes stretching. Normalized insertion loss decreases as the strain increases, and at higher frequencies, the amount of increase is greater. However, when the CPW is stretched to 65% and above, the overall shape of S-parameters changes indicating the open circuit of the CPW. Numerical models at different strain levels are also developed in CST Studio Suite to compare predictions with experimental data. It is seen in addition to geometry and conductivity changes in CPW that the dielectric constant of the substrate and the encapsulant and the surface roughness of the conductive silver ink need to be changed with stretching in the numerical model to be able to mimic the experimental data. With such changes, the numerical CPW simulation results match both the overall trend and the magnitude of insertion loss in measurement data.**

***Index Terms*— Coplanar waveguide (CPW), flexible hybrid electronics (FHE), monotonic stretching, numerical modeling.**

Manuscript received 4 May 2024; accepted 15 May 2024. Date of publication 4 June 2024; date of current version 16 August 2024. This work was supported by the Army Research Laboratory under Agreement W911NF-19-2-0345. Recommended for publication by Associate Editor X. Gu upon evaluation of reviewers' comments. *(Corresponding author: Yi Zhou.)*

Yi Zhou, Justin H. Chow, and Suresh K. Sitaraman are with the George W. Woodruff School of Mechanical Engineering, Georgia Institute of Technology, Atlanta, GA 30332 USA (e-mail: yzhou342@gatech.edu; justin.chow@gatech.edu; suresh.sitaraman@me.gatech.edu).

Manos M. Tentzeris is with the School of Electrical and Computer Engineering, Georgia Institute of Technology, Atlanta, GA 30332 USA (e-mail: etentze@ece.gatech.edu).

Color versions of one or more figures in this article are available at https://doi.org/10.1109/TCPMT.2024.3409526.

Digital Object Identifier 10.1109/TCPMT.2024.3409526

I. Introduction

FLEXIBLE hybrid electronics (FHE) is a system-level implementation of electronic devices that combines the mechanical advantage of flexible printed circuits and the reliable performance of silicon integrated circuits (ICs). The market size of FHE is expected to reach U.S. $77.3 billion in 2029, with various applications in healthcare, automotive, aerospace, agriculture, and consumer electronics [1], [2], [3], [4], [5], [6], [7], [8]. With the rising concept of Internet of Things (IoT) across these industries, the ability to support efficient and reliable data exchange through wireless communication is becoming an important design consideration for smart flexible devices, and in particular, wireless communication enabled by radio frequency (RF) technology is an important element of FHE applications [1], [2], [9], [10], [11], [12], [13], [14], [15], [16], [17], [18], [19], [20], [21], [22], [23], [24], [25], [26], [27], [28].

Printing technology, such as screen printing, inkjet printing, and aerosol jet printing, has been widely used for fabricating flexible electronics. It has clear advantages over traditional copper etched traces of low cost, wider material selection, not requiring clean room environment, and on-demand fabrication [1], [2], [29]. However, as an emerging fabrication technology, printing also brings uncertainty in reliability, especially as the working conditions of FHE always require various physical deformation. Therefore, research has been conducted in the reliability of printed electronics under deformation, including stretching, bending, and twisting [30], [31], [32], [33], [34], [35], [36], [37]. However, most of the works have investigated the performance of printed electronics under direct current (dc) conditions and used the change of resistance as a measure of reliability. In contrast, the performance of printed electronics under RF conditions is characterized by scattering parameters (S-parameters), which concern not only the change in the resistance of printed conductors but also the change in the overall geometry, dielectric properties of substrates, and the operating frequency band.

An interconnect or a transmission line is a ubiquitous and fundamental element in any RF system design, which

serves as the path that connects different components and modules. Therefore, it is necessary to study the performance of the interconnect in an FHE system in the RF regime alone under deformation. In FHE systems, traditional transmission line structures are used for the realization of planar interconnects. Typically, they are microstrip lines and coplanar waveguides (CPWs). They are successfully fabricated by different kinds of printing techniques depositing conductive ink onto polymer substrates [16], [17], [18], [19], [20], [21], [22], [23], [24], [25], [26]. Most of these reported studies have characterized the reliability of the RF performance by measuring S-parameters under bending as the only form of deformation. Since the strain induced by bending is low (about 1.3% when the bending radius is in the order of an inch [16]), the change in S-parameters due to monotonic bending is very minimal as observed. In contrast, the amount of strain that can be applied to the FHE by stretching is much higher than bending. Therefore, a greater amount of change in S-parameter can be expected due to strain-induced cracking, macroscopic geometry change, dielectric property change, and surface roughness change, which would be more severe due to stretching. There have been studies that have applied stretching to the flexible serpentine interconnects and have observed noticeable changes in S-parameters up to 4 GHz under stretching [27], [28]. However, the serpentine structures are known for reducing local strain, and the local strain across the whole structure is not uniform [38]. Instead, a uniform local strain that is equal to the applied global strain can be expected when stretching a traditional straight transmission line sample, which in comparison to a serpentine interconnect structure has a better RF performance to start with and normally has a higher maximum operating frequency. The scarcity of experimental data and numerical models in the RF regime up to above 20 GHz of traditional transmission line structure due to stretching has motivated the investigation presented in this work. The understanding of the RF performance change of the transmission line structure due to stretching would form a foundation for further investigation of the behavior of more complex RF modules under stretching and other kinds of deformation. Once the effect of stretching on a transmission line is understood, it is then possible to study transmission line-fed antennas and to deconvolute the antenna performance alone by knowing the performance of transmission line.

In this work, a screen-printed transmission line, specifically a CPW transmission line, is designed, fabricated, and tested under monotonic stretching with a tested frequency range of 2–20 GHz. CPW is of interest in this work because it can be screen-printed in a single fabrication step as both the conductive signal trace and conductive ground are placed on the same side. As the conductive parts are on the same side of the substrates and fabricated in the same step, the effect due to stretching would be uniform among them, and therefore, an exclusive investigation on how monotonic stretching would impact the conductors leading to the change of S-parameters can be performed.

The goal of this work is to understand the RF performance of the CPW in 2–20 GHz under monotonic stretching using both experimental and modeling methods. Although conductors have been printed and stretched on various flexible and stretchable substrates such as polyimide (PI), polyethylene terephthalate (PET), thermoplastic polyurethane (TPU), polydimethylsiloxane (PDMS), and liquid crystal polymer (LCP), this work focuses on printed conductors on PET substrate. In general, substrates, such as PI and PET, have a higher modulus and lower stretchability in the range of 50%–80% strain, while substrates, such TPU and PDMS, have a much lower modulus and higher stretchability up to 150% strain. For the intended RF applications for conformal attachment to automotive panels, aircraft body, protective helmets, and body supports, the strains are usually in the range of 15%–25%, and thus, the evaluation of RF performance of printed conductors on PET substrate is particularly relevant. Furthermore, in these applications, the temperature and other environmental conditions are harsh, and thus, substrates, such as PET, are appropriate for further study and discussion. The CPW in this work is composed of a PET substrate with screen-printed silver conductor, and a protective encapsulation layer is deposited on top of the conductor to prevent unwanted damage and shortage from the stretching fixtures to the conductors. A set of custom fixtures has been developed to be used with a universal testing machine to perform the monotonic stretching test. In situ S-parameters of the encapsulated CPW are measured by a vector network analyzer (VNA) through the monotonic stretching test up to 70% strain when failure occurs in the signal trace and is visually confirmed. Numerical models in CST[1] Studio Suite (referred to as CST in the later context) are developed to facilitate the understanding of how stretching affects the RF performance by impacting the geometries and material properties.

II. Encapsulated CPW Design

Fig. 1 shows the dimensioned schematic design of the encapsulated CPW sample fabricated by DuPont.[1] The selected materials for the sample are commercially available due to the fundamental requirement for consistency, repeatability, and professional quality. The focus of this article is not the synthesis and processing of new materials. Instead, the focus is to understand the RF performance of printed transmission line under extensive stretching. The design is a traditional CPW design with a dielectric encapsulation layer on top. Both the signal trace and the side ground planes are screen-printed to DuPont PET substrate with DuPont 5028 ink. DuPont 5028 ink is a silver-flake ink in an acrylic-based polymer matrix, with the volume fraction of silver to be approximately around 70%. The ink layer is designed to have a thickness of 10 μm, and the substrate is 125 μm thick. The sample is rolled through a calendar press to enhance the conductivity of the conductive ink, following its printing. From previous experimental experience, it is learned that a dielectric encapsulant layer can prevent unwanted damage to the ink from the fixture. Also, the encapsulant will help against potential shorting issue from the SMA connector. Thus, the CPW is encapsulated with a 26-μm DuPont 5018 dielectric layer. Through in-house simulations,

[1]Trademarked.

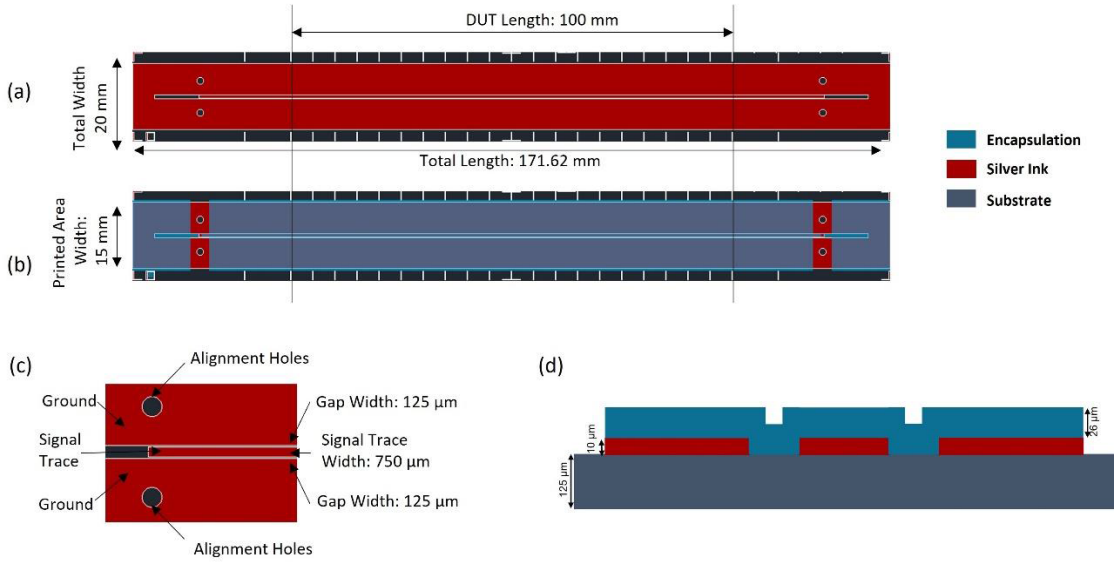

Fig. 1. Dimensioned schematic design details of the encapsulated CPW. (a) Top–down view of silver ink layer on PET substrate without encapsulation layer. (b) Top–down view of encapsulation layer on silver ink layer that is on PET substrate. (c) Top–down zoomed-in view of the signal and ground trace design without encapsulation layer. (d) Cross-sectional view of the encapsulated CPW.

it is seen that the encapsulation layer adds an additional loss of about 0.02 dB/mm through the operating frequency range investigated in this study. Since the loss introduced by the encapsulation is small and the focus of this study is to determine the relationship between physical deformation to the RF performance of the screen-printed ink, the study with such an encapsulated design is performed to minimize potential interference and contamination during the testing process, so that the accuracy and reliability of our results can be ensured. It is also noticed that adding the encapsulation would change the characteristic impedance of the CPW, so that when designing the signal trace width and the gaps between the trace and the ground plane, the impact from the encapsulation is included.

Another constraint when designing the geometry of the CPW comes from the vertical launches that are used to interface between the CPW and the cables connected to the VNA. Fairview Microwave[1] FMCN1476 2.92-mm vertical launch connectors are used as they can be well incorporated into the stretching fixtures and setup, which will be discussed in Section III. The launch connectors have a cut-out in the body in order to prevent shorting the signal line, and the CPW signal width and gap sizes should fit in the cut-out. Therefore, an optimal design of the CPW is given as follows. It has a signal trace width of 750 μm and gaps between the signal trace and the ground planes of 125 μm. The sample is designed to have a total length of 171.62 mm and a total width of 20 mm, as shown in Fig. 1. The length that would be subjected to stretching is 100 mm in the middle, and the rest of the portions near the ends are used for clamp-down during the stretching test and are not subject to any strain. In other words, the device under testing (DUT) in this work is the 100-mm-long encapsulated CPW. Therefore, the connections to the vertical launches on both sides are outside of the stretching length. The alignment holes for the screw attachment of the vertical launches are also drawn on the substrate as indicated.

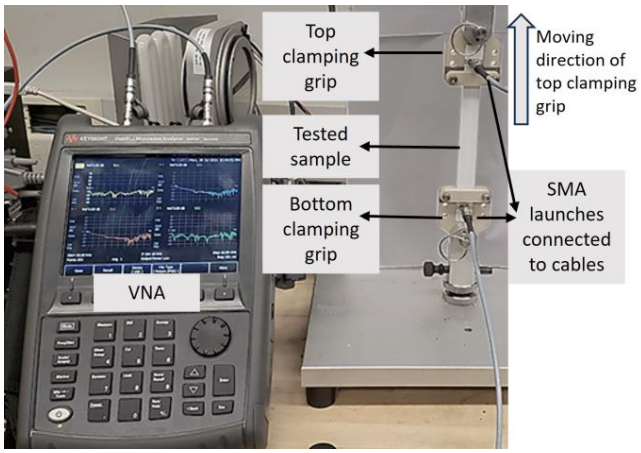

Fig. 2. Schematics of the monotonic stretching test setup.

The S-parameters measurements of the fabricated samples are presented in Section III-C.

III. Experimental Work

A. Stretching Test Fixtures and Setup

The stretching test is performed with a universal testing machine, and a pair of custom clamping grips are manufactured for the CPW sample, as shown in Fig. 2. To prevent slipping of the plastic film, 800-grit SiC abrasive paper is glued to both sides of the gripping. Grips are designed to secure both the CPW sample and the SMA vertical launches in the stretching test. For a secured electrical connection between the CPW and the vertical launches, a third cut-out hole is designed in the clamping grips for the screw to go through from the back to push the substrate into the center pin of the launch connector. The clamping grips are made of polyether ether ketone (PEEK), which has good mechanical and electrical properties.

As illustrated in Fig. 2, once the CPW sample is clamped down to the grips, it is hooked up to a Test Resources 100 Series universal testing machine and a VNA. All the S-parameters measurements in this work are taken by a FieldFox[1] N9918A VNA, and the measurements are obtained in the range of 2–20 GHz. Prior to conducting the test, the VNA is first calibrated using the complete two-port short-open-load-through (SOLT) calibration method and a Keysight[1] 85 561 A calibration kit [39]. The reference plane is established at the end of the cables. Following calibration, the S-parameters measurement of the CPW sample is first taken at unstretched position. Then, the sample undergoes stretch testing, as the bottom clamping grip remains stationary and the top clamping grip travels upward, as indicated in Fig. 2. In this work, the elongation of the sample is quantified by strain, as $\varepsilon = (l - l_0/l_0) \times 100\%$, where ε is the strain, l is the total length of DUT after stretching, and l_0 is the initial length of DUT, which is 100 mm. The stretching rate is controlled by a testing machine with stretching occurring at a rate of 10 mm/min and pausing at 1% strain intervals to measure the S-parameters of the sample. The measurement is taken until the S-parameters measurement shows significant shape changes and signal trace breakage is visually confirmed in the sample, which occurs at 70% strain as in this case. The pauses during the stretching process for electrical measurement last for under a minute, on average.

B. Deembedding Methodology

Since the DUT of this work is the 100-mm encapsulated CPW, the effects introduced by the clamping fixture, SMAs, and the additional length of CPW (on both sides of the sample as shown in Fig. 2) can be removed from the measurements, using a 2x-thru structure. The diagram of the 2x-thru deembedding method described in [40] is presented in Fig. 3. Fig. 3(a) shows the total structure that includes the CPW, the clamping sections and vertical launch SMAs on both sides, and the additional material past the SMAs. Fig. 3(b) shows the standard structure that includes only the clamping sections and ports on both sides and the additional material past the ports. In order for the 2x-thru method to be applied, it is necessary to identify the DUT and the 2x fixtures. As indicated in Fig. 3(a), the DUT is the 100-mm CPW at the center of the tested sample; 1x fixture, Fixture A, would include the clamping section on the left and the left vertical launch SMA, and the additional material past the left SMA; and the other 1x fixture, Fixture A', is identical to Fixture A, while it is on the right side of the sample. Thus, in Fig. 3(b), the standard structure can be seen as one 1x fixture, Fixture A, and the other 1x fixture, Fixture A', and they are connected with a zero-length thru structure. As seen, the 2x-thru standard structure used in this work would require a shorter encapsulated CPW, as presented in Fig. 3(c). Such shorter CPW is designed and fabricated in the same fashion as the full-length sample described in Section II. The S-parameters of the 2x-thru standard structure shown in Fig. 3(b) are recorded by the calibrated VNA and then are used to deembed the raw S-parameters measurements taken in the stretching test using a commercial tool, Amphenol[1] CISS De-embedding Utility [41].

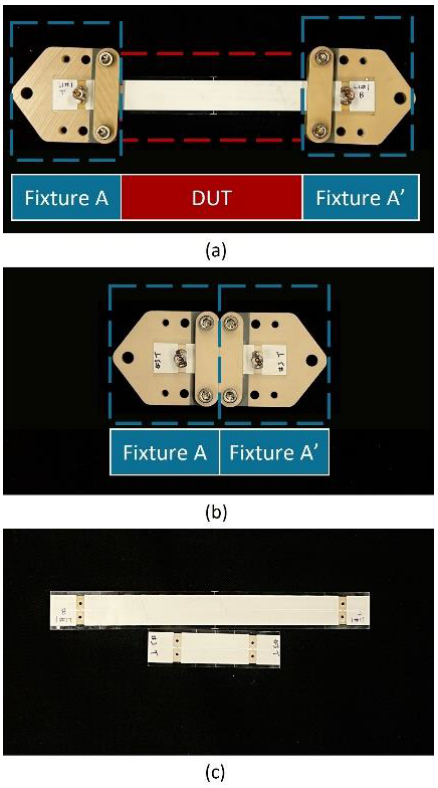

Fig. 3. Schematics of 2x-thru deembedding method. (a) Total structure, (b) standard structure, and (c) customized shorter CPW (bottom) used in standard structure in comparison to the tested CPW (top).

When the CPW undergoes stretching, the sample portions within Fixtures A and A' experience no strain and other physical changes as they are tightly and securely clamped down by the grips. No slippage and movement are expected of the sample under the fixtures. Thus, when the SMA connectors are made to contact the pads on the sample through the fixtures, the SMA connectors continue to be in contact with the pads throughout the experiment with no misalignment or slippage. Therefore, the S-parameters of the 2x-thru standard structures shown in Fig. 3(b) can be used to deembed all the measurement data from 0% to 70% strain of stretching.

C. Experimental Results

The deembedded S-parameters results (S11 and S21) of the CPW under monotonic stretching are presented in Fig. 4. In the plots, the initial unstrained measurement is in dark blue, and the final measurement at 70% strain is in dark red. The line color changes based on the strain level as indicated on the color bar on the right of the plots. As seen in Fig. 4(a), the unstrained return loss of the CPW is greater than 12 dB at most tested frequencies. The return loss shows minor changes until 65% strain when the sample is no longer functional. At 65% strain, the magnitude of return loss flattens out to 0 dB. It is worth mentioning that the substrate is plastically deformed but remains unbroken even when subjected to a 70% strain; instead, some breaks occur in the screen-printed signal trace at some point along its length, which causes the open circuit. The open circuit at 65% indicates large cracks all the way across the width of the sample somewhere along the length.

The failure strain level aligns with the results in dc monotonic stretching work in the authors' lab of encapsulated screen-printed sample on PET substrate with a similar ink DuPont 5025. The return loss could potentially serve as an indication of a total mechanical failure of the CPW under stretching, as it flattens out when an open circuit happens. It is noticed that the return loss of the tested CPW is barely greater than 10 dB at certain frequencies. This is due to the challenge of having a good 50-Ω match. Several aspects contribute to this design challenge in flexible printed electronics. First, the edges of the printed conductor are not straight or clean due to nature of printing. The designed gap of the tested CPW between the transmission line and the two side ground planes is narrow for screen printing to accommodate the SMA connector. The contact between the transmission line and the SMA connectors is controlled by screws and may result in a poor contact interface. In addition, there is uncertainty of the ink conductivity, which is dependent on the surface roughness of the substrate and processing conditions. However, the purpose of this work is to study the change in S-parameters, starting with the initial condition whatever it may be, and thus, although the initial S11 is barely −10 dB, the change in S11 is the primary focus of this work.

In comparison to the return loss, the insertion loss shows a more pronounced trend in changes when the CPW undergoes monotonic stretching. The insertion loss plot in Fig. 4(b) is normalized to per unit length in the unit of dB/mm based on the stretched length of the DUT. In this way, the effect of the length difference of the CPW due to stretching is removed from the comparison. The unstrained length-normalized insertion loss is linearly increasing from 0.02 to 0.06 dB/mm as the frequency changes from 2 to 20 GHz. The insertion loss increases as the strain increases at all frequencies, and the overall shape of the insertion loss does not change until the strain reaches 65%, which is the same time when the return loss changes the overall shape and when possibly the open circuit happens. When the strain reaches 65%, the normalized insertion loss is greater than 0.20 dB/mm.

The length-normalized insertion loss is replotted in Fig. 5 against the strain at six selected frequencies: 2, 4, 8, 12, and 18 GHz. These frequencies are chosen because they are the beginning and ending frequencies of designated frequency bands of S, C, X, and Ku for radar, terrestrial, and satellite applications. As seen, below 65% strain, the magnitude of changes of the return loss at each frequency is different, the higher the frequency the greater amount changes. At 2 GHz, the insertion loss increases from 0.02 to 0.11 dB/mm from 0% to 64% strain, while at 18 GHz, the insertion loss increases from 0.06 to 0.22 dB/mm from 0% to 64% strain. At each given frequency, the relationship between the magnitude of the insertion loss and strains between 0% and 64% when CPW is functional is well captured by a linear function, $y = ax + b$, where y is the value of the insertion loss per unit stretched length and x is the applied strain. The fit parameters a and b with R^2 values are presented in Table I. Generally, the R^2 values to all six fit linear lines are high, especially for the first five counting from the lower frequencies to the higher frequencies, whose R^2 are all above 0.99. The fit linear line

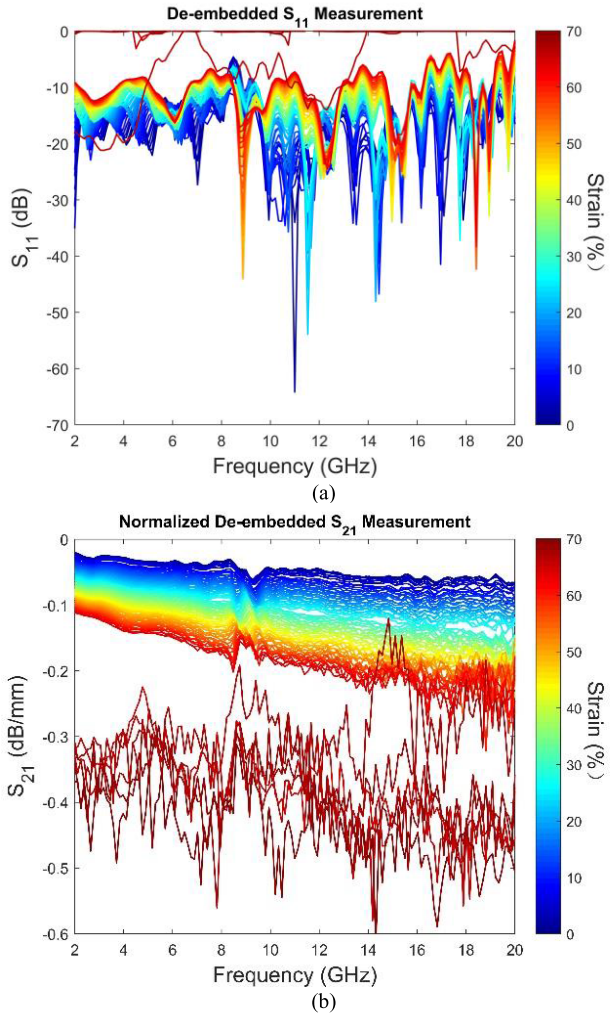

Fig. 4. In situ (a) S11 and (b) length-normalized S21 measurement of CPW under monotonic stretching from 0% to 70% strain.

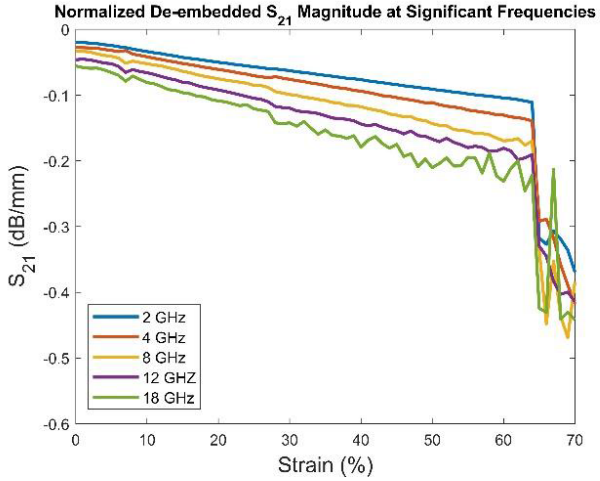

Fig. 5. Length-normalized S21 measurement results of CPW under monotonic stretching from 0% to 70% strain at key frequencies against strains.

to the highest selected frequency of 18 GHz has a smaller R^2 of 0.9757, which is caused by the oscillation of original insertion loss measurements after around 30% strain. Noticeable oscillations are also observed at the plots of 8 and 12 GHz after

TABLE I
FIT PARAMETERS FOR THE LINEAR RELATIONSHIP BETWEEN THE MAGNITUDE OF INSERTION LOSS AND STRAINS

Frequency	a	b	R^2
2 GHz	0.1425	0.0199	0.9984
4 GHz	0.1772	0.0244	0.9987
8 GHz	0.2248	0.0302	0.9981
12 GHz	0.2419	0.0442	0.9959
18 GHz	0.2787	0.0546	0.9757

around 30% strain but to a lesser extent. It can be concluded that the insertion loss at higher frequencies is more sensitive to the strain experienced by the transmission line. This is closely related to the microstructure changes in the printed silver ink due to stretching. The polymer-supported printed silver conductor would have local necking and cracking due to monotonic stretching, and once the cracks are formed, the cracks would grow in length, width, and depth as the strain increases [30], [31], [42], [43]. Therefore, it is expected that the surface roughness of the conductor will become larger as the strain increases. Since the skin depth requirement is in reverse relation to the square root of the operating frequency, at higher frequencies, the signal is distributed more to the surface of the conductor, and therefore, RF response at higher frequencies is more sensitive to the topology change induced by the crack formation.

IV. NUMERICAL SIMULATION

Numerical models are developed to establish correlations between the experimental measurements of S-parameters across the frequency range of 2–20 GHz as the strain level is increased from 0% to 70%. The geometry and conductivity are among the necessary parameters for the accurate modeling of the RF performance, and the actual geometry and conductivity measurements at each of the tested strain levels are used as inputs to these parameters. Changes in the width and thickness of the sample at various strain levels are expected since a body undergoing stretching in the axial direction would also experience strain in its transverse directions due to the Poisson effect. Usually, the conductivity of any screen-printed silver conductive strip decreases as the axial strain increases. With the actual geometry and conductivity of the tested sample accounted for, the modeling effort could yield a more accurate comparison between experimental measurements and predictions on the RF performance under strain.

A. Unstrained Model Setup in CST

First the unstrained computer-aided design (CAD) model of the encapsulated CPW is built in CST to reflect the three-layer structures shown in Fig. 1 and other design details discussed in Section II. The CPW model has a PET substrate at the bottom, screen-printed silver conductors in the middle, and a dielectric layer on top of the conductor. The ink is measured to have a conductivity of 2.985×10^6 S/m, which is very close to the value listed by the manufacturer [44], and the equivalent isotropic dielectric material properties used are presented in Table II.

TABLE II
DIELECTRIC MATERIAL PROPERTIES

Material	Dielectric Constant	Loss Tangent
PET Substrate	2.90 [45]	0.008 [46]
DuPont™ 5018 Encapsulation	4.40 [47]	0.050*

* Loss tangent is fitted from CST model.

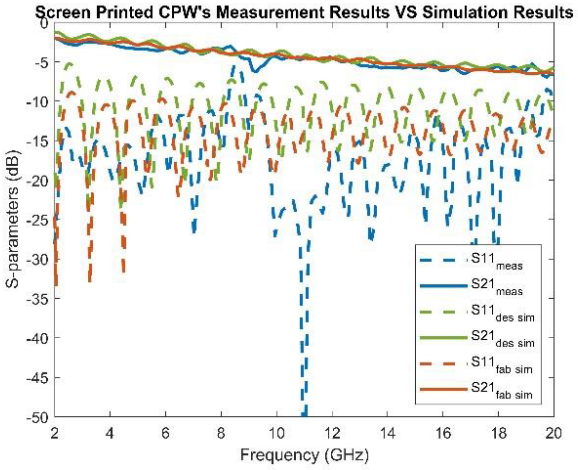

Fig. 6. 100-mm-long CPW S-parameters of CST simulation built with designed geometry and fabrication result geometry in comparison to CPW S-parameters measurement results.

Fig. 6 shows the comparison of the deembedded unstrained measurement results to the simulation results, where the blue lines represent the deembedded S-parameters measurement of the fabricated sample, and the green lines represent the simulated S-parameters of the original design. The measured insertion loss shows good agreement with the simulation results based on the original design, but the return loss shows more than a 5-dB difference. Since using numerical modeling to investigate the stretching impact on the CPW is one of the aims of this work, a well-correlated base model at the unstrained condition needs to be established. The geometry of the model is then corrected based on the fabrication results, which is expected to have some discrepancies from the designed parameters due to the limitation of screen-printing and the nature of the small feature sizes in the CPW. An additional CPW sample without the encapsulation layer is prepared for feature size measurement of the screen-printed silver conductive layer. The width of the signal trace is measured to be 793.1 μm, and the gap width is measured to be 86.7 μm. The thickness of the signal trace is measured by a Dektak[1] 150 Profilometer. The scan is made sure to cover not only the signal trace but also the gaps on both sides so that the measured elevation in the two gaps can be used as the zero-elevation reference point. The average step height over the signal width taken from the profilometer measurement result is 9.8 μm. The surface roughness of the printed ink is also measured by the profilometer, and the measurement shows that the surface roughness is 1.3 μm root mean square (rms), which is comparable to the value reported in [31]. The deviation

TABLE III
CPW GEOMETRY DESIGNED VALUES

CPW Design Parameter	Designed Value (μm)	Fabrication Results (μm)
Signal Trace Width	750.0	793.1
Gap Width	125.0	86.7
Conductor Layer Thickness	10.0	9.8

between the fabricated sample and the design parameters is summarized in Table III. By updating the geometry in the CST model, the orange S-parameters plots in Fig. 6 representing the fabrication simulation results show a better correlation to the measurement data. Some other geometry parameters that are used to build the original unstrained encapsulated CPW model in CST are a total substrate width of 20 mm, a DUT length of 100 mm, an encapsulation thickness of 26 μm, and an encapsulation width of 15 mm.

B. Strained Model Setup in CST With Geometry and Conductivity Change

The base model is parametrized so that the geometries can be updated in the seven strained models. To reflect the dimensions changes of the DUT due to stretching in the seven strained models, the DUT length is increased according to

$$L(\varepsilon) = (L_0) \cdot (1 + \varepsilon) \tag{1}$$

where L is the length of the CPW, L_0 is the initial length, and ε is the strain in the axial direction. All other lateral dimensions are decreased according to

$$w(\varepsilon) = (w_0) \cdot (1 + \varepsilon)^{-\nu} \tag{2}$$

where w is the width or thickness parameter of interest, w_0 is the initial width or thickness, and ν is Poisson's ratio. Poisson's ratio of PET is measured to be 0.48 at 70% strain by axially stretching a bare PET and measuring the decreasing width, and it is assumed to be the same value at all strain levels.

From previous dc monotonic stretching work with a similar ink DuPont 5025 of Chow et al. [48], the conductivity of the screen-printed silver-flake ink is found to decrease as the conductive strip undergoes monotonic stretching. DuPont 5025 has the same formulation as DuPont 5028, but with slightly lower volume fraction of silver. The conductivity change due to stretching is taken from the dc work of DuPont 5025 and adapted to the seven strained models. Table IV summarizes both geometry parameters and ink conductivity values that are used in all eight models. Therefore, the CST models at different strain levels reflect the combination of the geometry changes and conductivity changes due to stretching. The dielectric materials are first assumed to have no property changes due to stretching, which means that the dielectric properties presented in Table II are applied in all models.

C. Simulation Results and Further Updates in Dielectric Properties

Both the unstrained and the strained CPW models are simulated in the time solver of CST. The normalized simulated S21 plots are presented in Fig. 7 in a green dashed-dotted line, with the comparison to the deembedded measurement results in a blue solid line. The simulated insertion loss per unit length shows the same trend as the measurement that it decreases as the strain increases at all frequencies. However, the magnitude of decrease shown in simulation is less than the magnitude of decrease in the measurement. As the strain level increases, there are more discrepancies between the values obtained from simulations and measurements. In other words, the measurement data are more lossy than the simulation results, and the greater the strain level, the more lossy the measurements are compared to the simulation results.

One of the potential reasons that cause the differences between the results from the simulations and the data from the measurements is the possible change in the dielectric property of the substrate due to stretching. The dielectric constant of polymers is strongly related to their molecular structure. The higher the polarizability of the material, the greater the value of the dielectric constant [49], and the greatest dielectric constant is measured along the preferred molecular chain alignment direction in the crystalline region [50], [51]. As the polymer film experiences uniaxial stretching, the molecular chain will orientate more along the tensile stretching direction, therefore resulting in an increase in the dielectric constant [52], [53], [54], [55]. Previous work has shown a continuous increase in the refractive index along the tensile loading direction of PET up to 20% strain, while no significant change is shown in the transverse direction [55]. By the Maxwell relation [56], the dielectric constant equals the square of the optical refractive index, and thus, the increase in the refractive index indicates an increase in the dielectric constant as well. Therefore, a continuous increase in the equivalent dielectric constant is expected in the PET films at least up to 20% strain in this study. From 20% to 70% strain of stretching, the remaining testing region of this study, the continuous increase of the dielectric constant of PET is also expected as no crystallinity change due to stretching is expected prior to 150% of strain [57], indicating that no major crystalline transformation occurs in the film. Second, the linear strain hardening effect in the stress–strain curve of PET film continues to 90% strain after the yield strain at 2.5% [55], which also indicates that no major polymer crystalline transformation occurs [54]. A similar trend of the dielectric constant change is assumed for the encapsulation polymer layer in this work. According to a previous study [51], a maximum of 10% increase in the dielectric constant of PET is observed as a 350% strain is applied to the film, and therefore, less than this percentage increase in the dielectric constants is expected in our work. By increasing the equivalent dielectric constant values in the CST model, the insertion loss becomes more lossy; however, with even up to 10% increase of the dielectric constant, there is only 0.006-dB/mm additional loss added to the insertion loss of the 40% stretch model, and there is still a significant difference between the simulation results and the experimental data. Another dielectric property,

TABLE IV
GEOMETRIES AND INK CONDUCTIVITY VALUES USED IN DIFFERENT STRAIN LEVELS OF CST MODELS

Strain Level (%)	0	10	20	30	40	50	60	70
Signal Trace Width (um)	793.1	757.6	726.6	699.3	674.8	652.8	632.9	614.8
Signal Trace Thickness (um)	9.8	9.4	9.0	8.6	8.3	8.1	7.8	7.6
Gap Width (um)	86.7	82.8	79.4	76.4	73.8	71.4	69.2	67.2
Substrate Thickness (um)	125	119.4	114.5	110.2	106.4	102.9	99.8	96.9
Substrate Width (mm)	20	19.1	18.3	17.6	17.0	16.5	16.0	15.5
CPW Length (mm)	100	110	120	130	140	150	160	170
Encapsulation Width (mm)	15	14.3	13.7	13.2	12.8	12.3	12.0	11.6
Encapsulation Thickness (um)	26	24.8	23.8	22.9	22.1	21.4	20.7	20.2
Ink Conductivity ($\times 10^5$ S/m)	29.85	9.965	6.001	4.419	3.393	2.680	2.136	0.086

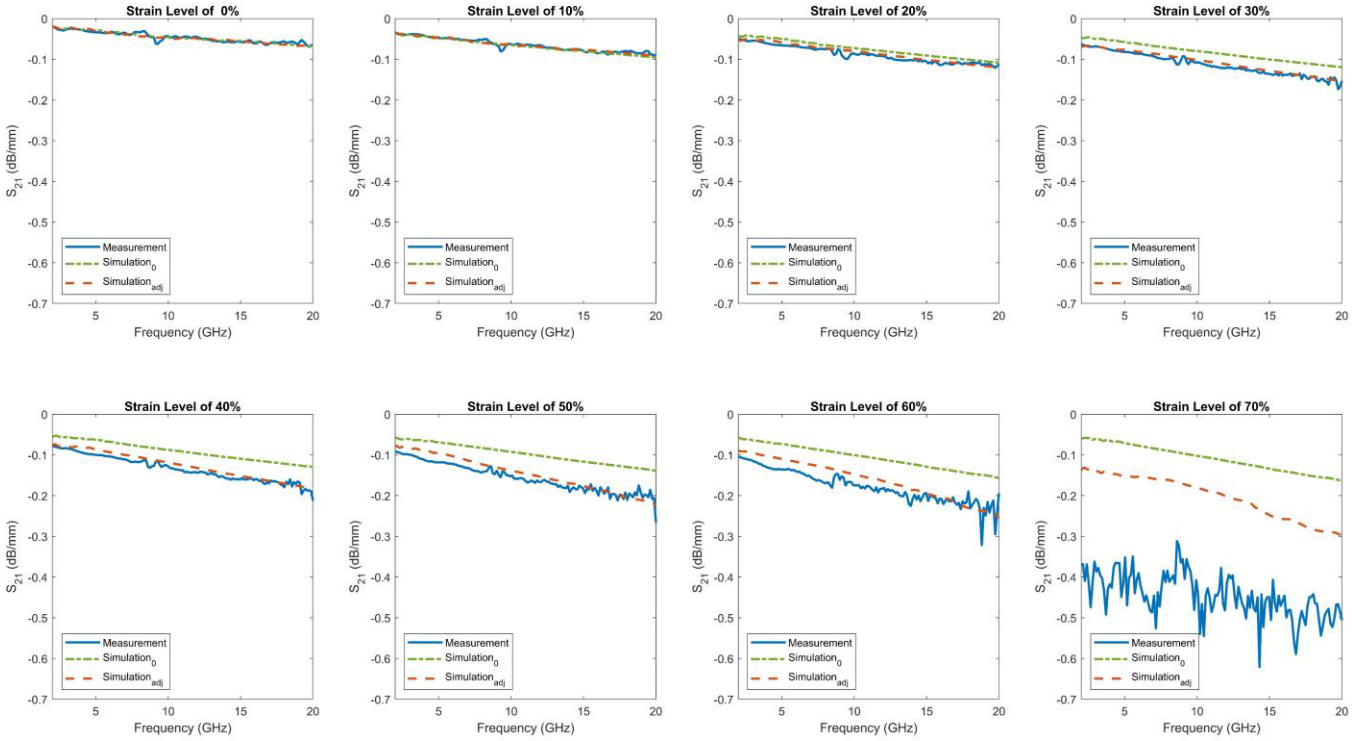

Fig. 7. CST simulation results in comparison to measurement results in 0%–70% strain levels.

loss tangent of the polymers, is found to have an inverse relationship with the degree of crystallinity in the polymer [49], [51], [58], [59]. However, no crystallinity change is expected when the polymer is stretched to only 70%, and thus, the loss tangent of the PET is not expected to change in this study, which matches the data reported at room temperature up to 170% strain in a previous dielectric study of PET [59].

The other limitation of the model constructed in CST is that the silver ink layer is built as an ideal noncracked metal blocks. In previous dc monotonic stretching test done on similar material set, microstructure changes in conductor and cracking effects [43] as well as the dc resistance changes under stretching [48] have been reported. It is found that the decrease in the conductivity (or the increase in resistivity under stretching) of the screen-printed silver ink is a result of fracture or cracks in the conductor due to stretching. However, as shown in Section IV-B, updating only the conductivity value of the silver ink layer to account for such cracking is not sufficient to capture the overall change in the RF performance. The stretching of the conductor would also impact the surface

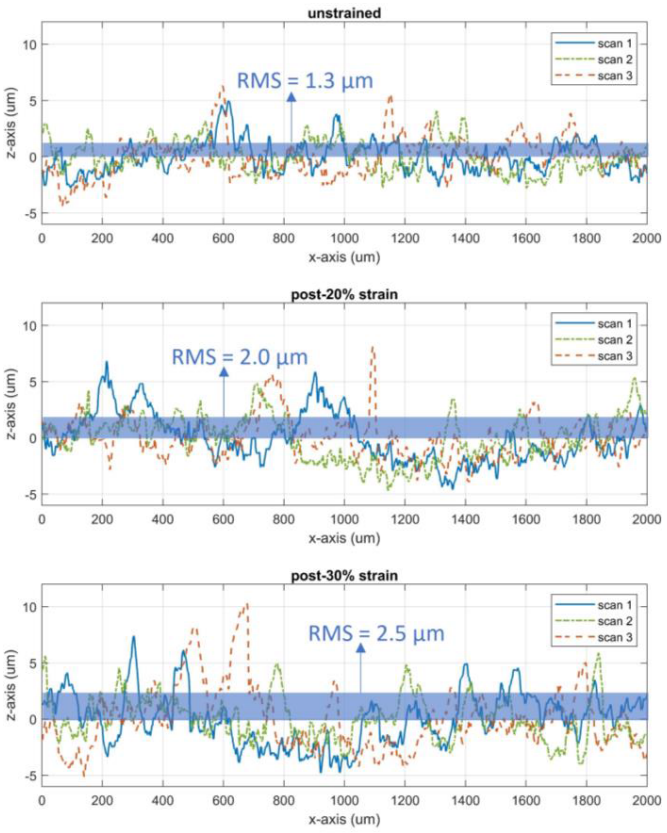

Fig. 8. Surface roughness measurement results of the screen-printed silver ink conductor on PET substrate at unstrained, post-20% strain, and post-30% strain conditions.

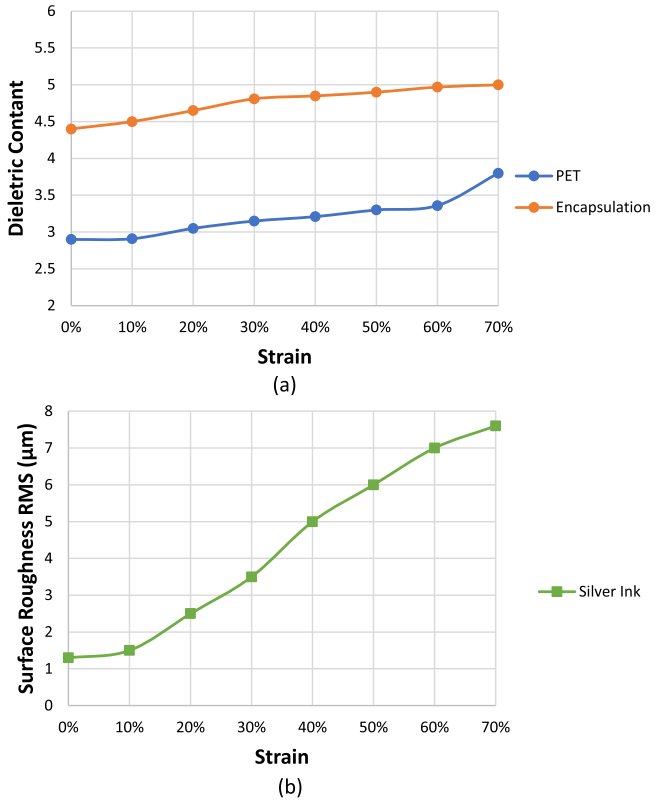

Fig. 9. Adjusted properties applied in different strain levels of CST models of (a) dielectric constant of dielectrics and (b) surface roughness rms of the silver ink conductor.

roughness as mentioned in Section III-C, and the higher the strain values, the conductor experienced, greater its surface roughness would be. The surface roughness measurement data of the printed silver ink conductor shown in Fig. 8 verified this finding. The samples used for the surface roughness measurements are silver conductors of DuPont 5028 screen printed onto PET substrate. The post-20% and 30% strain samples are stretched to the corresponding strain value by the universal testing machine and held for 30 min before being released for surface roughness measurement. The surface roughness measurements are taken by the Dektak 150 Profilometer with a stylus having radius of 2 μm. The flexible samples are double-taped to a wafer, which is then secured to the testing stage of the profilometer. For each sample, three scans are taken at different locations over 2000 μm in length along the stretching direction. In Fig. 8, the x-axis represents the length along the scan direction, and the z-axis represents the height of the surface relative to the mean height of corresponding scan. RMS is a representation of the surface roughness, which is calculated by RMS $= (()/)1/2\sum_{i=1}^{n}(z_i - z_{\text{mean}})^2 n$, where n is the number of measurement point, z_i is the surface height at each measurement point, and z_{mean} is the mean surface height across the scan. The rms values reported in Fig. 8 are the average of the three scans. It is clearly seen that as the sample experiences the tensile strain from 0% to 20% and to 30%, the average surface roughness rms increases from 1.3 to 2.0 μm and to 2.5 μm. Since the surface roughness measurements are taken at 0% strain after stretching to 20% or 30%, the data may be considered "post situ," and thus, the values would be less than the in situ surface roughness values of the silver ink under stretching. Therefore, increasing the surface roughness value of the silver ink layer in the CST model is also necessary to fully capture the stretching impact. It is worth mentioning that 30% is the maximum strain that the silver ink on PET can undergo without difficulty for the flexible substrate to remain coplanarity, which is the key for a profilometer scan. In addition, because the stylus of the profilometer needs a flat, solid, and secure plane to land on, it is also too challenging to measure an in situ strained surface roughness measurement of the silver ink.

In addition to the geometry change and conductivity updates, increases are applied to the dielectric constants of the polymers and the surface roughness values of the silver ink of CPW in CST models. The modified values applied to the CST simulation are presented in Fig. 9. Such numerical models predict well the comprehensive stretching effects that a CPW would experience on the insertion loss as indicated in the orange dashed lines in Fig. 7 up to 60% strain. Both the overall trend and the overall magnitude of insertion loss agree with the experimental data. In the 60% strain model, the dielectric constant values of the PET substrate and encapsulation layer are 3.36 and 4.97, respectively, which are 113% and 115%, respectively, of the original value at unstrained conditions. The surface roughness rms value of the silver ink layer is adjusted to 7.0 μm in the 60% strain model, which is 538% of the

original value at the flat condition. At a 70% strain level, when catastrophic cracks have appeared (around 65% strain) in the silver ink, the simulated insertion loss is not able to capture the shape of the measured insertion loss regardless of how much the properties are increased. As seen, the adjusted surface roughness values of silver ink at 20% strain and 30% strain models are slightly higher than the corresponding post-strain measurements reported in Fig. 9(b) as expected. As the strain increases, the adjusted surface roughness of the silver ink applied in the model is getting closer to the signal trace (silver ink) thickness since the surface roughness increases and the thickness decreases. Although the surface roughness value is a macroscopic uniform change for the entire signal trace, while microstructure changes, such as cracks, are local in the ink, in the 60% strain model, the surface roughness rms of the silver ink of 7.0 μm that is comparable to the silver ink thickness value of 7.8 μm, indicating that some deep cracks are happening in the signal silver ink layer. However, when the local catastrophic cracking occurs in the ink through thickness and across the width to the signal trace beyond 65% strain, the uniform change of surface roughness rms in addition to other parameter changes in the CST model will not capture the undulations in the experimental data.

From the simulation result, it can be concluded that by combining changes in geometry, the conductivity of the conductor, the dielectric constant of polymers due to stretching, and the surface roughness rms value of the silver ink that reflects the formation of cracks, the impact of stretching on the CPW can be accurately predicted by the CST numerical model prior to the physical failure point. The focus of the future work would be to verify whether the changes of the dielectric constant and surface roughness due to stretching fit to this CPW work can be applied to some other RF elements such as an antenna, as for an antenna element, the operating frequency, the bandwidth, and efficiency would be affected by these contributing factors under stretching; and both experimental and modeling effort will be included. The current model assumes uniform conductivity, geometry, dielectric constant, and surface roughness changes across the entire sample length. In reality, however, local resistivity where cracks occur may be several orders of magnitude higher than the resistivity elsewhere in the conductor. One way to improve the CST model in future work is to provide the ability to create different resistivity values and/or surface roughness values at certain locations along the length to indicate cracks. A fatigue stretching test would be conducted to further study the reliability of the CPW; the mean strain and the amplitude of the fatigue test would be chosen based on the monotonic stretching test results in this work. Although adding the encapsulation layer in sample design helps with the experimental integrity in this work, it contributes to the RF performance of the sample and makes it hard to elucidate how monotonic stretching is impacting encapsulation and the PET substrate separately. In addition, the encapsulation layer prevents in situ optical failure observation on the silver ink. Therefore, future experiment and research will be conducted on silver ink with single type of polymer.

V. Conclusion

This work aims to understand the behavior of transmission lines under extreme stretching over a frequency range of 2–20 GHz, and the work has accomplished its objectives through models and simulations. The work also has provided insight into the behavior of the transmission lines under such extreme stretching through exploring dielectric constant changes and surface roughness of the printed conductor changes. In this work, an encapsulated screen-printed CPW is designed and fabricated. The RF performance of the CPW under monotonic stretching up to the physical failure point is characterized and measured. Electrical FEA models are developed to incorporate the geometry change of CPW and conductivity change of the ink layer due to stretching to the RF performance of the encapsulated CPW. Additional loss induced by dielectric molecular structure change and conductor crack formation from stretching is added to the simulation models by adjusting the dielectric constant of the dielectric layers and surface roughness rms of the conductive silver ink layer, respectively.

The designed sample is a traditional CPW design with an encapsulation layer on top of the conductive layer to prevent signal shorting issue during the stretching test. The conductive layer is screen-printed silver ink, and the substrate is PET. The sample design is optimized for the mechanical stretching test. The DUT length of the CPW that would be subjected to stretching is 100 mm. A pair of custom clamping grids are developed for the stretching test with RF measurements. The sample is stretched at a rate of 10 mm/min by a universal testing machine and pauses at 1% strain intervals to measure the S-parameters of the sample from 0% to 70% strain. S-parameters are measured by a VNA from 2 to 20 GHz.

The measured S-parameters are deembedded by the 2x-thru method. The overall change of the return loss is observed to be minor until the strain reaches 65% where the return loss flattens out to 0 dB across all tested ranges. The overall shape of the insertion loss does not change until the strain reaches 65%, and unlike the return loss, the change in the insertion loss shows a clear trend as the CPW experiences the strains. More evaluation of insertion loss is performed with the length-normalized data in dB/mm based on the stretched length of the CPW. Such normalization prevents the lengthy design of the sample from obscuring the interpretation of test results and removes the effect of different lengths of the DUT. The normalized insertion loss increases as the strain increases at all frequencies, but at higher frequencies, a greater amount of decrease occurs in the normalized insertion loss. The relationship between the magnitude of the normalized insertion loss at selected frequencies versus the strain values up to 64% is linear, with some oscillation observed beyond 8 GHz, and the higher the frequency the greater the extent of oscillation. Before the conductor fails at some point around 65%, insertion loss is more sensitive to strain at higher frequencies because, at higher frequencies, the skin depth is smaller, which means at higher frequencies, there is less tolerance for the surface roughness change due to the formation of cracks. Finally, when the strain reaches 65%, the physical failure point when catastrophic cracking is happening somewhere along the conductor,

the normalized insertion loss is greater than 0.2 dB/mm at all frequencies.

CST simulations are developed to establish correlations between the experimental measurements. First, the actual geometry changes of the CPW and the conductivity change of the ink due to stretching are included in the models. Eight simulation models are run at strain levels between 0% and 70% with 10% increments. These models are capable of capturing the increasing trend shown in insertion loss measurements. The increase in equivalent isotropic dielectric constant in polymers is expected due to the molecular chain rearrangement along the stretching direction. The increase in the surface roughness of the conductive silver ink layer due to stretching is also observed. The model with increased dielectric constant of the dielectric layers and surfacer roughness of the conductive layer, in addition to overall geometry and conductivity changes, can successfully predict the full behavior of the CPW when undergoing monotonic stretching up to the failure point. These geometry and material property changes can be further verified by applying them into other RF component designs with the same material set and fabrication method that undergoes monotonic stretching in the future. The other focus of the future work would be to introduce local property changes to represent the crack in the 3-D model so that the comparison can be conducted with the model performed in this work. In addition, the fatigue stretching test would be conducted to further study the reliability of CPW. More future work would be conducted on a silver ink layer with a single type of polymer material.

ACKNOWLEDGMENT

This material is based on research sponsored by Army Research Laboratory under agreement number W911NF-19-2-0345. The U.S. Government is authorized to reproduce and distribute reprints for Government purposes notwithstanding any copyright notation thereon. The views and conclusions contained herein are those of the authors and should not be interpreted as necessarily representing the official policies or endorsements, either expressed or implied, of Army Research Laboratory (ARL) or the U.S. Government.

REFERENCES

[1] R. Das and X. He, *Flexible, Printed and Organic Electronics 2019–2029: Forecasts, Players & Opportunities*. Cambridge, U.K.: IDTechEx Research, 2019.

[2] Y. Khan, A. Thielens, S. Muin, J. Ting, C. Baumbauer, and A. C. Arias, "A new frontier of printed electronics: Flexible hybrid electronics," *Adv. Mater.*, vol. 32, no. 15, Apr. 2020, Art. no. 1905279, doi: 10.1002/adma.201905279.

[3] J. van den Brand et al., "Flexible and stretchable electronics for wearable health devices," *Solid-State Electron.*, vol. 113, pp. 116–120, Nov. 2015.

[4] Y. Ma et al., "Flexible hybrid electronics for digital healthcare," *Adv. Mater.*, vol. 32, no. 15, Apr. 2020, Art. no. 1902062, doi: 10.1002/adma.201902062.

[5] A. Eid et al., "Nanotechnology-empowered flexible printed wireless electronics: A review of various applications of printed materials," *IEEE Nanotechnol. Mag.*, vol. 13, no. 1, pp. 18–29, Feb. 2019.

[6] S. Khan, L. Lorenzelli, and R. S. Dahiya, "Technologies for printing sensors and electronics over large flexible substrates: A review," *IEEE Sensors J.*, vol. 15, no. 6, pp. 3164–3185, Oct. 2015.

[7] V. Misra et al., "Flexible technologies for self-powered wearable health and environmental sensing," *Proc. IEEE*, vol. 103, no. 4, pp. 665–681, Apr. 2015.

[8] M. Stoppa and A. Chiolerio, "Wearable electronics and smart textiles: A critical review," *Sensors*, vol. 14, no. 7, pp. 11957–11992, Jul. 2014.

[9] G. Yang et al., "A health-IoT platform based on the integration of intelligent packaging, unobtrusive bio-sensor, and intelligent medicine box," *IEEE Trans. Ind. Informat.*, vol. 10, no. 4, pp. 2180–2191, Nov. 2014.

[10] K. Hu, Y. Zhou, S. K. Sitaraman, and M. M. Tentzeris, "Fully additively manufactured flexible dual-band slotted patch antenna for 5G/mmWave wearable applications," in *Proc. IEEE Int. Symp. Antennas Propag. USNC-URSI Radio Sci. Meeting (AP-S/URSI)*, Jul. 2022, pp. 878–879.

[11] L. Portilla et al., "Wirelessly powered large-area electronics for the Internet of Things," *Nature Electron.*, vol. 6, pp. 10–17, Dec. 2022, doi: 10.1038/s41928-022-00898-5.

[12] K. Niotaki et al., "RF energy harvesting and wireless power transfer for energy autonomous wireless devices and RFIDs," *IEEE J. Microw.*, vol. 3, no. 2, pp. 763–782, Apr. 2023, doi: 10.1109/JMW.2023.3255581.

[13] J. Bito et al., "Millimeter-wave ink-jet printed RF energy harvester for next generation flexible electronics," in *Proc. IEEE Wireless Power Transf. Conf. (WPTC)*, Taipei, Taiwan, May 2017, pp. 1–4, doi: 10.1109/WPT.2017.7953871.

[14] Y. Zhou et al., "Study of electrical and mechanical characteristics of inkjet-printed patch antenna under uniaxial and biaxial bending," in *Proc. IEEE 69th Electron. Compon. Technol. Conf. (ECTC)*, May 2019, pp. 1939–1945, doi: 10.1109/ECTC.2019.00298.

[15] Y. Zhou, S. Sivapurapu, M. Swaminathan, and S. K. Sitaraman, "Mechanical and high-frequency electrical study of printed, flexible antenna under deformation," *IEEE Trans. Compon., Packag., Manuf. Technol.*, vol. 10, no. 7, pp. 1088–1100, Jul. 2020, doi: 10.1109/TCPMT.2020.2995532.

[16] Y. Zhou, K. Hu, M. M. Tentzeris, and S. K. Sitaraman, "Mechanical and Ka-band electrical reliability testing of interconnects in 5G wearable system-on-package designs under bending," in *Proc. IEEE 72nd Electron. Compon. Technol. Conf. (ECTC)*, May 2022, pp. 914–923, doi: 10.1109/ECTC51906.2022.00149.

[17] N. A. Amoli et al., "Screen-printed flexible coplanar waveguide transmission lines: Multi-physics modeling and measurement," in *Proc. IEEE 69th Electron. Compon. Technol. Conf. (ECTC)*, Las Vegas, NV, USA, May 2019, pp. 249–257, doi: 10.1109/ECTC.2019.00044.

[18] S. Sivapurapu et al., "Multi-physics modeling characterization of aerosol jet printed transmission lines," in *IEEE MTT-S Int. Microw. Symp. Dig.*, Reykjavik, Iceland, Aug. 2018, pp. 1–4, doi: 10.1109/NEMO.2018.8503509.

[19] Y. Shi, Z. Jiang, S. Lam, M. Leach, J. Wang, and E. G. Lim, "Multi-GHz microstrip transmission lines realised by screen printing on flexible substrates," in *Proc. IEEE Electr. Design Adv. Packag. Syst. Symp. (EDAPS)*, Dec. 2017, pp. 1–3, doi: 10.1109/EDAPS.2017.8277038.

[20] S.-M. Sim, Y. Lee, H.-L. Kang, K.-Y. Shin, S.-H. Lee, and J.-M. Kim, "RF performance of ink-jet printed microstrip lines on rigid and flexible substrates," *Microelectron. Eng.*, vol. 168, pp. 82–88, Jan. 2017, doi: 10.1016/j.mee.2016.11.011.

[21] B. K. Tehrani, B. S. Cook, and M. M. Tentzeris, "Inkjet-printed 3D interconnects for millimeter-wave system-on-package solutions," in *IEEE MTT-S Int. Microw. Symp. Dig.*, May 2016, pp. 1–4, doi: 10.1109/MWSYM.2016.7540084.

[22] M. Abt et al., "Aerosol-printed highly conductive Ag transmission lines for flexible electronic devices," *IEEE Trans. Compon., Packag., Manuf. Technol.*, vol. 8, no. 10, pp. 1838–1844, Oct. 2018, doi: 10.1109/TCPMT.2018.2869977.

[23] F. Cai, Y.-h. Chang, K. Wang, W. T. Khan, S. Pavlidis, and J. Papapolymerou, "High resolution aerosol jet printing of D-band printed transmission lines on flexible LCP substrate," in *IEEE MTT-S Int. Microw. Symp. Dig.*, Jun. 2014, pp. 1–3, doi: 10.1109/MWSYM.2014.6848597.

[24] M. M. Belhaj, W. Wei, E. Pallecchi, C. Mismer, I. Roch-jeune, and H. Happy, "Inkjet printed flexible transmission lines for high frequency applications up to 67 GHz," in *Proc. 44th Eur. Microw. Conf.*, Oct. 2014, pp. 1528–1531, doi: 10.1109/EuMC.2014.6986740.

[25] S. Myllymaki, J. Putaala, J. Hannu, H. Jantunen, M. Mantysalo, and E. Kunnari, "Failure mode characterization in inkjet-printed CPW lines utilizing a high-frequency network analyzer and post-processed TDR analysis," *Prog. Electromagn. Res. C*, vol. 43, pp. 1–14, 2013, doi: 10.2528/pierc13052104.

[26] X. Huang, T. Leng, K. H. Chang, J. C. Chen, K. S. Novoselov, and Z. Hu, "Graphene radio frequency and microwave passive components for low cost wearable electronics," *2D Mater.*, vol. 3, no. 2, May 2016, Art. no. 025021, doi: 10.1088/2053-1583/3/2/025021.

[27] U. Stehr, L. F. Centeno, Y. Ni, H. O. Jacobs, and M. A. Hein, "RF properties of stretchable transmission line structures," in *Proc. German Microw. Conf. (GeMiC)*, Cottbus, Germany, Mar. 2020, pp. 272–275.

[28] B. Huyghe, H. Rogier, J. Vanfleteren, and F. Axisa, "Design and manufacturing of stretchable high-frequency interconnects," *IEEE Trans. Adv. Packag.*, vol. 31, no. 4, pp. 802–808, Nov. 2008, doi: 10.1109/TADVP.2008.927811.

[29] J. Wiklund et al., "A review on printed electronics: Fabrication methods, inks, substrates, applications and environmental impacts," *J. Manuf. Mater. Process.*, vol. 5, no. 3, p. 89, Aug. 2021, doi: 10.3390/jmmp5030089.

[30] G. Cahn, O. Pierron, and A. Antoniou, "Electrical performance evolution and fatigue mechanisms of silver-filled polymer ink under uniaxial cyclic stretch," *Flexible Printed Electron.*, vol. 6, no. 3, Sep. 2021, Art. no. 035008, doi: 10.1088/2058-8585/ac1243.

[31] G. Cahn, A. Barrios, S. Graham, J. Meth, A. Antoniou, and O. Pierron, "The role of strain localization on the electrical behavior of flexible and stretchable screen printed silver inks on polymer substrates," *Materialia*, vol. 10, May 2020, Art. no. 100642, doi: 10.1016/j.mtla.2020.100642.

[32] O. Glushko, P. Kraker, and M. J. Cordill, "Explicit relationship between electrical and topological degradation of polymer-supported metal films subjected to mechanical loading," *Appl. Phys. Lett.*, vol. 110, no. 19, May 2017, Art. no. 191904, doi: 10.1063/1.4982802.

[33] I. A. Bower, C. L. Taylor, and S. K. Sitaraman, "Study of inkjet-printed serpentine structure on flexible substrates deformed over sculptured surfaces," *Flexible Printed Electron.*, vol. 5, no. 1, Feb. 2020, Art. no. 015010.

[34] B. Stewart and S. Sitaraman, "Biaxial inflation stretch test for printed flexible electronics," *Adv. Eng. Mater. Adv. Eng. Mater.*, vol. 23, no. 6, Jun. 2021, Art. no. 2001503.

[35] R. Chen, J. H. Chow, Y. Zhou, J. S. Meth, and S. K. Sitaraman, "Cyclic bending effects on resistance of screen-printed silver conductors," *IEEE Trans. Compon., Packag., Manuf. Technol.*, vol. 11, no. 11, pp. 1877–1888, Nov. 2021, doi: 10.1109/TCPMT.2021.3108491.

[36] R. Chen, J. Chow, C. Taylor, J. Meth, and S. Sitaraman, "Adaptive curvature flexure test to assess flexible electronic systems," in *Proc. IEEE 68th Electron. Compon. Technol. Conf. (ECTC)*, May 2018, pp. 236–242, doi: 10.1109/ECTC.2018.00044.

[37] J. H. Chow, J. Meth, and S. K. Sitaraman, "Twist testing for flexible electronics," in *Proc. IEEE 69th Electron. Compon. Technol. Conf. (ECTC)*, May 2019, pp. 785–791, doi: 10.1109/ECTC.2019.00124.

[38] C. Ye, R. Chen, and S. K. Sitaraman, "An automatic numerical approach to optimize flexible serpentine structure design," *Flexible Printed Electron.*, vol. 7, no. 2, Jun. 2022, Art. no. 025011, doi: 10.1088/2058-8585/ac6ea7.

[39] (2012). *Understanding VNA Calibration*. Accessed: Jan. 18, 2019. [Online]. Available: http://anlage.umd.edu/Anritsu_understanding-vna-calibration.pdf

[40] B. Chen et al., "Multi-ports 2×-thru de-embedding: Theory, validation, and mode conversion characterization," *IEEE Trans. Electromagn. Compat.*, vol. 61, no. 4, pp. 1261–1270, Aug. 2019, doi: 10.1109/TEMC.2019.2908782.

[41] *ACS/ITRL De-embedding Software | Amphenol CS*. Accessed: Jun. 22, 2023. [Online]. Available: https://www.amphenol-cs.com/

[42] Q. Li, A. Antoniou, and O. Pierron, "Understanding resistance increase in composite inks under monotonic and cyclic stretching," *Flexible Printed Electron.*, vol. 7, no. 4, Dec. 2022, Art. no. 045010, doi: 10.1088/2058-8585/aca98a.

[43] G. Cahn, "Understanding the electrical response to applied strain of polymer supported screen printed inks," Ph.D. dissertation, George W. Woodruff School Mech. Eng., College Eng., Georgia Inst. Technol., Atlanta, GA, USA, 2021. [Online]. Available: http://hdl.handle.net/1853/65072

[44] *DuPont 5028 Silver Conductor Technical Data Sheet*. Accessed: Jun. 22, 2023. [Online]. Available: https://www.dupont.com/content/dam/dupont/amer/us/en/mobility/public/documents/en/5028.pdf

[45] *Melinex ST506 Datasheet*. Accessed: Aug. 4, 2023. [Online]. Available: http://52.167.112.238/FilmEnterprise/Datasheet.asp?ID=271&amp

[46] B. Cami. *Dielectric Characterization of Mylar Films and the Effects of Doping Processes*. Accessed: Jun. 22, 2023. [Online]. Available: https://www.osti.gov/servlets/purl/1412076

[47] *Dupont 5018 UV Curable Dielectric Technical Data Sheet*. Accessed: Jun. 22, 2023. [Online]. Available: https://www.dupont.com/content/dam/dupont/amer/us/en/mobility/public/documents/en/EI-10177-DuPont-5018-UV-Curable-Dielectric.pdf

[48] J. H. Chow et al., "Stretch testing of flexible electronics," in *Proc. FLEX*, Monterey, CA, USA, 2018.

[49] J. Wei, R. Delgado, M. C. Hawley, and M. T. Demeuse, "Dielectric analysis of semi-crystalline poly(ethylene terephthalate)," *MRS Proc.*, vol. 347, 1994, doi: 10.1557/proc-347-735.

[50] S. Osaki and K. Tashiro, "Molecular orientation and dielectric anisotropy in polyimide films as determined by the microwave method," *Macromolecules*, vol. 31, no. 5, pp. 1661–1664, Mar. 1998, doi: 10.1021/ma961713y.

[51] S. Osaki, "Dielectric anisotropy of stretched poly(ethylene terephthalate) at microwave frequencies," *J. Appl. Phys.*, vol. 64, no. 8, pp. 4181–4186, Oct. 1988, doi: 10.1063/1.341332.

[52] L. Lin and A. S. Argon, "Structure and plastic deformation of polyethylene," *J. Mater. Sci.*, vol. 29, no. 2, pp. 294–323, 1994, doi: 10.1007/bf01162485.

[53] I. M. Fouda and M. M. El-Tonsy, "Studies on the molecular structure of vestan fibers due to cold drawing," *Polymer-Plastics Technol. Eng.*, vol. 45, no. 2, pp. 223–229, Mar. 2006, doi: 10.1080/03602550500373832.

[54] B. Clauss and D. R. Salem, "A chain-intrinsic fluorescence study of orientation-strain behavior in uniaxially drawn poly(ethylene terephthalate) film," *Macromolecules*, vol. 28, no. 24, pp. 8328–8333, Nov. 1995, doi: 10.1021/ma00128a049.

[55] Z. Zhou et al., "Strain-optical behavior of polyethylene terephthalate film during uniaxial stretching investigated by Mueller matrix ellipsometry," *Polymer*, vol. 182, Nov. 2019, Art. no. 121842, doi: 10.1016/j.polymer.2019.121842.

[56] D. L. Grigsby, D. H. Johnson, M. Neuberger, and S. J. Welles, "Electronic properties of materials," in *Electronic Properties of Materials*. New York, NY, USA: Springer-Verlag, 1967.

[57] M. Matsuo, M. Tamada, T. Terada, C. Sawatari, and M. Niwa, "Deformation mechanism of poly(ethylene terephthalate) film under uniaxial stretching," *Macromolecules*, vol. 15, no. 4, pp. 988–998, Jul. 1982, doi: 10.1021/ma00232a009.

[58] S. Osaki, "High temperature dielectric loss of poly(ethylene terephthalate) films at microwave frequency," *Polymer*, vol. 35, no. 1, pp. 47–49, Jan. 1994, doi: 10.1016/0032-3861(94)90047-7.

[59] L.-W. Wong, "Dielectric loss of stretched polyethylene terephthalate," Ph.D. dissertation, Division Phys., Chin. Univ. Hong Kong, Hong Kong, 1974. [Online]. Available: https://core.ac.uk/download/pdf/48562849.pdf

Yi Zhou received the B.S. and M.S. degrees in mechanical engineering from Georgia Institute of Technology, Atlanta, GA, USA, in 2017 and 2019, respectively. She is currently pursuing the Ph.D. degree in mechanical engineering from the Georgia Institute of Technology, Atlanta, Georgia.

She has been a member of the Computer-Aided Simulation Packaging Reliability (CASPaR) Laboratory, Georgia Tech, since 2017.

Ms. Zhou is the winner of the SMTA Charles Hutchins Educational Grant of 2021. She was also one of the recipients of the EPS ECTC Student Travel Grant Awards 2022 with her article.

Justin H. Chow received the B.S. and M.S. degrees in mechanical engineering, the M.S. degree in civil engineering (structural), and the Ph.D. degree in mechanical engineering from Georgia Institute of Technology, Atlanta, GA, USA, in 2009, 2014, 2016, and 2022, respectively.

He is currently a Research Engineer with Georgia Tech. His research in electronic packaging has included lead-free solder microstructure, electrical/thermal compliant interconnects, and flexible electronics.

Manos M. Tentzeris (Fellow, IEEE) received the Diploma degree (Suma Cum Laude) from the National Technical University, Athens, Greece, in 1992, and the M.S. and Ph.D. degrees in electrical engineering and computer science from the University of Michigan, Ann Arbor, MI, USA, in 1993 and 1998, respectively.

He was a Visiting Professor with the Technical University of Munich, Munich, Germany, in 2002; GTRI-Ireland, Athlone, Ireland, in 2009; and LAAS-CNRS, Toulouse, France, in 2010; and a Humboldt Guest Professor with FAU, Nuremberg, Germany, in 2019. He is currently the Ed and Pat Joy Chair Professor with the School of Electrical and Computer Engineering, Georgia Institute of Technology, Atlanta, GA, USA, where he heads the ATHENA Research Group (20 researchers). He was the Head of the GT ECE Electromagnetics Technical Interest Group, Georgia Electronic Design Center Associate Director of RFID/Sensors Research, Georgia Institute of Technology NSF-Packaging Research Center Associate Director of RF Research, and the RF Alliance Leader. He has helped to develop academic programs in 3-D/inkjet-printed RF electronics and modules, flexible electronics, origami and morphing electromagnetics, highly integrated/multilayer packaging for RF, millimeter wave, sub-terahertz, and wireless applications using ceramic and organic flexible materials, paper-based RFID's and sensors, wireless sensors and biosensors, wearable electronics, "green" and transient electronics, energy harvesting and wireless power transfer, nanotechnology applications in RF, microwave MEMs, and SOP-integrated (UWB, multiband, mmW, and conformal) antennas. He has authored more than 850 papers in refereed journals and conference proceedings, seven books, and 26 book chapters.

Dr. Tentzeris is a member of the URSI-Commission D, the MTT-15 Committee, and the Technical Chamber of Greece; an Associate Member of EuMA; and a fellow of the Electromagnetic Academy. He was a recipient/co-recipient of the 2024 Georgia Tech Outstanding Achievement in Research Innovation Award; the 2023 Proceedings of IEEE Best Paper Award; the 2022 Georgia Tech Outstanding Doctoral Thesis Advisor Award; the 2021 IEEE Antennas and Propagation Symposium (APS) Best Student Paper Award; the 2019 Humboldt Research Prize; the 2017 Georgia Institute of Technology Outstanding Achievement in Research Program Development Award; the 2016 Bell Labs Award Competition Third Prize; the 2015 IET Microwaves, Antennas, and Propagation Premium Award; the 2014 Georgia Institute of Technology ECE Distinguished Faculty Achievement Award; the 2014 IEEE RFID-TA Best Student Paper Award; the 2013 IET Microwaves, Antennas and Propagation Premium Award; the 2012 FiDiPro Award in Finland; the iCMG Architecture Award of Excellence; the 2010 IEEE Antennas and Propagation Society Piergiorgio L.E. Uslenghi Letters Prize Paper Award; the 2011 International Workshop on Structural Health Monitoring Best Student Paper Award; the 2010 Georgia Institute of Technology Senior Faculty Outstanding Undergraduate Research Mentor Award; the 2009 IEEE TRANSACTIONS ON COMPONENTS AND PACKAGING TECHNOLOGIES Best Paper Award, the 2009 E. T. S. Walton Award from the Irish Science Foundation; the 2007 IEEE AP-S Symposium Best Student Paper Award; the 2007 IEEE MTT-S IMS Third Best Student Paper Award; the 2007 ISAP Poster Presentation Award; the 2006 IEEE MTT-S Outstanding Young Engineer Award; the 2006 Asia–Pacific Microwave Conference Award; the 2004 IEEE TRANSACTIONS ON ADVANCED PACKAGING Commendable Paper Award; the 2003 NASA Godfrey "Art" Anzic Collaborative Distinguished Publication Award; the 2003 IBC International Educator of the Year Award; the 2003 IEEE CPMT Outstanding Young Engineer Award; the 2002 International Conference on Microwave and Millimeter-Wave Technology Best Paper Award, Beijing, China; the 2002 Georgia Institute of Technology–ECE Outstanding Junior Faculty Award; the 2001 ACES Conference Best Paper Award; the 2000 NSF CAREER Award; and the 1997 Best Paper Award of the International Hybrid Microelectronics and Packaging Society. He was the General Co-Chair of the 2023 IEEE Wireless Power Transfer Technology Conference and Expo (WPTCE) in San Diego and the 2019 IEEE APS Symposium in Atlanta. He was the TPC Chair of the IEEE MTT-S IMS, Symposium and the Chair of the 2005 IEEE CEM-TD Workshop. He is the Vice-Chair of the RF Technical Committee (TC16) of the IEEE CPMT Society. He is the Founder and the Chair of the RFID Technical Committee (TC24) of the IEEE MTT-S and the Secretary/Treasurer of the IEEE C-RFID. He served as an Associate Editor for IEEE TRANSACTIONS ON MICROWAVE THEORY AND TECHNIQUES, IEEE TRANSACTIONS ON ADVANCED PACKAGING, and the *International Journal of Antennas and Propagation*. He has given more than 150 invited talks to various universities and companies all over the world. He is currently one of the IEEE EPS Distinguished Lecturer and served as one of the IEEE MTT-S Distinguished Microwave Lecturers and the IEEE CRFID Distinguished Lecturer.

Suresh K. Sitaraman received the B.Eng. degree in mechanical engineering from the University of Madras, Chennai, India, in 1982, the M.A.Sc. degree in mechanical engineering from the University of Ottawa, Ottawa, ON, Canada, in 1985, and the Ph.D. degree in mechanical engineering from The Ohio State University, Columbus, OH, USA, in 1989.

He is a Regents' Professor and a Morris M. Bryan, Jr. Endowed Professor with the George W. Woodruff School of Mechanical Engineering, Georgia Institute of Technology (Georgia Tech), Atlanta, GA, USA. His expertise is in the areas of microscale and nanoscale structure fabrication, testing and characterization, and physics-based modeling and reliable design, as applied to flexible and rigid microsystems. Prior to joining Georgia Tech in 1995, he was with IBM Corporation, Endicott, NY, USA. He has coauthored more than 340 journal and conference publications over the past few years. He has managed several research and development projects funded by U.S. federal agencies, industry, and other sources totaling millions of dollars, and has mentored a vast array of post-doctoral fellows and research engineers and doctoral, master's, bachelor's, and high-school students.

Dr. Sitaraman's work has been recognized through several awards and honors. Among them, he received the Distinguished Faculty Achievement Award from Georgia Tech/Mechanical Engineering in 2024, the Richard Chu Award for Excellence in Thermal and Thermo-Mechanical Management of Electronics, ITherm/IEEE-EPS in 2023, the Zeigler Outstanding Educator Award from Georgia Tech/Mechanical Engineering in 2019, the NextFlex Fellow recognition in 2018, the Outstanding Achievement in Research Program Development Award (Team Leader) from Georgia Tech in 2017, the ASME/EPPD (Electronic and Photonic Packaging Division) Applied Mechanics Award in 2012, and the Thomas French Achievement Award from the Department of Mechanical and Aerospace Engineering, The Ohio State University, in 2012. He received the Sustained Research Award from Georgia Tech—Sigma Xi in 2008 and the Outstanding Faculty Leadership Award for the Development of Graduate Research Assistants, Georgia Tech, in 2006. His coauthored papers have won the Commendable Paper Award from IEEE TRANSACTIONS ON ADVANCED PACKAGING in 2004 and the Best Paper Award from IEEE TRANSACTIONS ON COMPONENTS AND PACKAGING TECHNOLOGIES in 2001 and 2000. He also received the Metro-Atlanta Engineer of the Year in Education Award in 1999 and the NSF-CAREER Award in 1997. He serves as an Associate Editor for IEEE TRANSACTIONS ON COMPONENTS, PACKAGING, AND MANUFACTURING TECHNOLOGY.